APPLIED PHYSICS

A reflective millimeter-wave photonic limiter

Rodion Kononchuk[1,2], Suwun Suwunnarat[2], Martin S. Hilario[3], Anthony E. Baros[3], Brad W. Hoff[3], Vladimir Vasilyev[4], Ilya Vitebskiy[4], Tsampikos Kottos[2], Andrey A. Chabanov[1]*

Millimeter-wave (mm-wave) communications and radar receivers must be protected from high-power signals, which can damage their sensitive components. Many of these systems arguably can be protected by using photonic limiting techniques, in addition to electronic limiting circuits in receiver front-ends. Here we demonstrate, experimentally and numerically, a free-space, reflective mm-wave limiter based on a multilayer structure involving a nanolayer of vanadium dioxide VO_2, which experiences a heat-related insulator-to-metal phase transition. The multilayer acts as a variable reflector, controlled by the incident wave intensity. At low intensities VO_2 remains dielectric, and the multilayer exhibits strong resonant transmittance. When the incident intensity exceeds a threshold level, the emerging metallic phase renders the multilayer highly reflective while safely dissipating a small portion of the input power, without damage to the limiter. In the case of a Gaussian beam, the limiter has a nearly constant output above the limiting threshold input.

INTRODUCTION

Millimeter-wave (mm-wave) is a valuable network and sensing technology that uses frequency bands in between 30 and 300 GHz (*1*–*3*). Operating in this spectral range has important advantages over lower-frequency bands. Not only do mm-waves allow larger bandwidths to transmit data at multigigabit speeds (*4*), but they also provide higher spatial resolution due to shorter wavelengths, which can be exploited for a variety of accurate sensing applications (*5*). At the same time, mm-waves are more readily scattered by small, millimeter-sized particles and stronger absorbed by moisture and oxygen present in the atmosphere. Thus, mm-wave signals work best with line-of-sight propagation and at frequencies falling within atmospheric electromagnetic transparency windows (at about 35, 94, 140, and 220 GHz).

In recent decades, there has been growing attention to the threat of high-power microwaves (HPM) to electronic systems, including radio communications and radar receivers (*6*–*8*). HPM sources nowadays can reach peak powers of 1 GW in short pulses of ~0.1 μs at repetition rates of several 100 Hz or average powers of 100 kW at frequencies from 1 to more than 100 GHz (*9*, *10*). At sufficiently high power densities, the effects of HPM on electronics may result in failure or even permanent damage of the circuits, because of thermal effects (*7*). In this regard, the receiver is particularly vulnerable, because it contains highly sensitive electronics such as low-noise amplifier (LNA), while the attached antenna provides a front door for HPM to couple into the system. PIN-diode power limiters (*11*), introduced between the antenna and LNA, cannot protect the receiver from the front-door coupling. Moreover, they are best suited for lower frequencies (≤15 GHz) (*12*) and are prone to overheating, which can be particularly damaging in highly integrated systems enabled by short wavelength of mm-waves. On the bright side though, the size of system components required to receive and process mm-wave signals is small enough to allow using mature optical techniques (*13*–*19*), such as optical limiting.

Optical limiting is a technique to protect photosensitive devices from damage caused by intense optical radiation (*20*, *21*). Optical limiters are therefore designed to block high-intensity laser radiation while transmitting low-intensity light. Most passive optical limiters use materials with nonlinear absorption, which are transparent to low-intensity light but turn opaque if the light intensity exceeds a certain (limiting) threshold level (*22*–*24*). A typical passive limiter, however, absorbs a substantial portion of high-level radiation, which can cause overheating and damage to the limiter itself (*21*, *25*).

To overcome this problem, the concept of a reflective photonic limiter, which reflects rather than absorbs high-intensity radiation, has been introduced (*26*–*28*). A passive reflective photonic limiter involves a photonic bandgap structure, such as a multilayer cavity, incorporating a nonlinear (*28*, *29*) or a phase-change material (PCM) (*30*, *31*). At low intensities, the photonic structure displays a strong resonant transmittance. High-intensity radiation, however, forces nonlinearity to kick in or phase transition to be induced, producing an impedance mismatch resulting in a strong broadband reflectivity. The high reflectivity prevents the limiter from overheating, thereby greatly increasing the limiter damage threshold. Other important advantages of the photonic design include orders-of-magnitude larger extinction ratio (the ratio of transmittances below and above the limiting threshold) and the possibility to substantially lower the limiting threshold by adjusting the photonic structure hosting the nonlinear material or a PCM. The aforementioned approach thus provides advanced broadband protection from high-level radiation, although low-intensity transmission is essentially narrowband because of its resonant nature. Arguably, free-space mm-wave limiters can be designed in much the same way to protect system receivers from high-power signals and to allow the receivers to function normally when these high-power signals are not present.

Here, we report a free-space, reflective photonic limiter for the *W* band (75 to 110 GHz), inspired by recent optical designs. Our mm-wave limiter is based on a resonant multilayer structure incorporating a nanolayer of vanadium dioxide (VO_2), undergoing an insulator-to-metal phase transition when heated above the critical temperature of $\theta_c \approx 69$ ° C. Thus, we first discuss the design and fabrication of the multilayer structure and then investigate the mm-wave limiting properties of the multilayer by low-power spectral

[1]Department of Physics and Astronomy, University of Texas at San Antonio, San Antonio, TX 78249, USA. [2]Department of Physics, Wesleyan University, Middletown, CT 06457, USA. [3]Air Force Research Laboratory, Directed Energy Directorate, Kirtland AFB, NM 87117, USA. [4]Air Force Research Laboratory, Sensors Directorate, Wright-Patterson AFB, OH 45433, USA.
*Corresponding author. Email: andrey.chabanov@utsa.edu

measurements at successively increasing temperatures and by time-resolved continuous-wave (CW) measurements at high input powers. Our experimental results are then corroborated by three-dimensional (3D) MULTIPHYSICS simulations, which allow us to gain deeper insight into the limiting process by exploring the dynamics of the limiter driven by the VO_2 phase transition.

The approach based on the use of insulator-to-metal transition materials is highly scalable and can be replicated in any spectral range, from microwave (MW) to optical [see, for example, (*32*–*35*) and references therein]. At MW frequencies, however, the insulator-to-metal transition is accompanied by much greater change in the complex permittivity of the PCM—orders of magnitude in our case. This provides an unprecedented flexibility in control of the MW radiation flow, unattainable in optics.

RESULTS

Mm-wave limiter design and low-power measurements at varying temperature

The reflective mm-wave limiter studied in this work is illustrated in Fig. 1 (A and B). The limiter design involves a photonic bandgap structure constructed of 76.2-mm-diameter C-cut sapphire (Al_2O_3) wafers, with a 525-μm-thick wafer in the middle and four 256-μm-thick wafers on the sides, separated by air gaps of a uniform thickness of about 792 μm. The middle sapphire wafer is coated on one side with a polycrystalline VO_2 to a thickness of approximately 150 nm (see Materials and Methods and fig. S1). Measurements of sheet resistance of the VO_2 coating reveal an abrupt insulator-to-metal transition at ~67° C, with a four-orders-of-magnitude change in the sheet resistance over a temperature range of ~5° C (fig. S2). According to literature (*36*–*38*), in the transition region, the electrical and optical properties of thin-film VO_2 are determined by the volume fraction of the thin film transformed into the metallic phase.

The resonant setting of Fig. 1 (A and B) allows to enhance the limiter extinction ratio by orders of magnitude while markedly lowering the limiting threshold, as compared to that provided by a VO_2 layer on a substrate. Below θ_c, the multilayer structure exhibits resonant transmittance (with a resonance Q factor of 260) of the incident intensity I_0 at a frequency of the localized (defect) mode of $f_0 \approx 95$ GHz (see Fig. 1C). The spatial distribution of the electric field intensity within the multilayer at the resonance frequency is plotted with a solid red line in Fig. 1E. The position of the VO_2 layer (shown in green) coincides with an antinodal plane of the resonant electric field. The resonance conditions facilitate the initial mm-wave heating of the VO_2 nanolayer and the adjacent sapphire layer, resulting in a substantial lowering of the limiting threshold. When the VO_2 temperature exceeds θ_c, the multilayer turns highly reflective over the entire W band, as seen in Fig. 1D. Moreover, the metallic VO_2 layer (shown in orange in Fig. 1F) is now shielded from incident radiation by the multilayer front end. The latter substantially increases the limiter damage threshold. Note that the resonance Q factor defines both (i) the operational frequency range below θ_c, which is given by the full width at half maximum (FWHM) of the transmittance peak, FWHM = $\frac{f_0}{Q}$, and (ii) the resonant absorptance, which determines the limiting threshold. A reduction in the limiting threshold thus comes at a cost of narrower-band operation of the limiter. Away from the resonant frequency, the multilayer is highly reflective regardless of θ, leaving the VO_2 in dielectric state even at high incident intensity levels.

Since design and modeling of the photonic limiter requires accurate values of the dielectric properties of the constitutive materials, we perform mm-wave measurements of the sapphire and VO_2-on-sapphire wafers at low power (≤10 mW) and successively increased temperatures from 27° to 110° C (see Materials and Methods). The (ordinary) effective relative permittivity of sapphire in the W band, $\epsilon_s = 9.32 + i0.009$, is determined from measurements of insertion loss and phase of the sapphire wafer and remains unchanged on heating over the whole temperature range. Figure 2A shows the transmittance T (blue circles), reflectance R (black circles), and absorptance $A = 1-T-R$ (red circles) of the VO_2-on-sapphire wafer at 95 GHz (in the vicinity of the Fabry-Perot resonance of the substrate) as a function of increasing temperature. The phase transition in the VO_2 layer manifests itself as an abrupt drop in the transmittance accompanied by a steep increase in the reflectance and a sharp peak in the absorptance, because of marked change in the permittivity of VO_2 during the transition (see Fig. 2B). The effective relative permittivity,

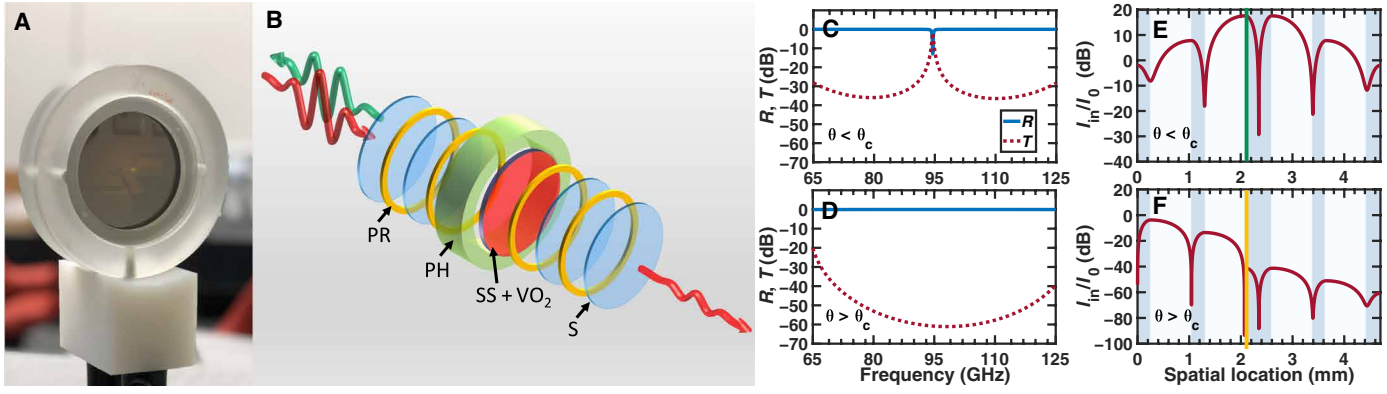

Fig. 1. Reflective mm-wave photonic limiter. A picture (**A**) and schematic (**B**) of the mm-wave photonic limiter consisting of 256-μm-thick (S) and 525-μm-thick (SS) sapphire wafers separated by 792-μm air-gap spacers (PR) and a 150-nm VO_2 layer deposited on the SS sapphire. The layer stack is retained in a plastic holder (PH). (**C** and **D**) Simulated transmittance T and reflectance R of the photonic structure at normal incidence, at $\theta > \theta_c$ (C) and $\theta < \theta_c$ (D). (**E** and **F**) Simulated internal intensity profiles in the direction of wave propagation of the incident intensity I_0 at the resonance frequency 95 GHz, at $\theta > \theta_c$ (E) and $\theta < \theta_c$ (F). Sapphire and air-gap layers are shown in dark and light blue, and the VO_2 layer in green and yellow at the lower and higher temperatures, respectively. Photo credit: Rodion Kononchuk, The University of Texas at San Antonio.

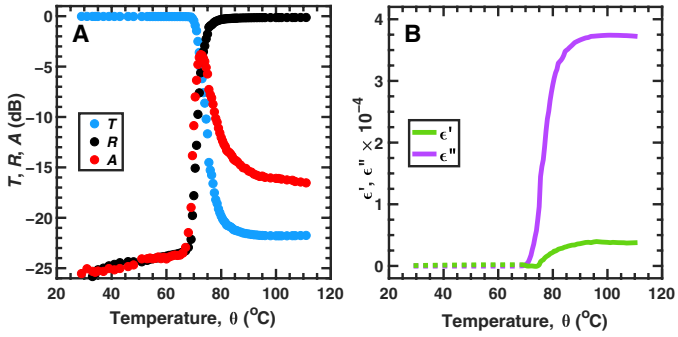

Fig. 2. Mm-wave dielectric properties of the VO_2 nanolayer at low input power and increasing temperature. (**A**) Mm-wave transmittance *T*, reflectance *R*, and absorptance *A* of the VO_2-on-sapphire wafer at 95-GHz input power of ≤10 mW and successively increasing temperature θ. (**B**) Temperature-dependent real (ϵ'_{VO2}) and imaginary (ϵ''_{VO2}) parts of the relative permittivity of the VO_2 layer at 95 GHz, determined from the measurements of the insertion loss and phase of the VO_2-on-sapphire wafer (solid lines) and transmittance measurements of the photonic limiter (dashed lines).

$\epsilon_{VO2} = \epsilon'_{VO2} + i\epsilon''_{VO2}$, is found by fitting the observed insertion loss and phase of the VO_2-on-sapphire wafer to those obtained from numerical simulations using 2 × 2 transfer-matrix formalism (*39*). The real and imaginary parts, ϵ'_{VO2} and ϵ''_{VO2}, obtained from the fit at $\theta \geq 69$ ° C are plotted with the increasing temperature by solid lines (in green and magenta, respectively) in Fig. 2B. Below 69° C, the VO_2 contribution to the insertion loss and phase is too small to be observed; it is observed, though, in mm-wave measurements of the photonic limiter that follow. The corresponding ϵ'_{VO2} and ϵ''_{VO2} are shown by the dashed lines in Fig. 2B.

According to Fig. 2A, the VO_2-on-sapphire wafer can act as a temperature-controlled mm-wave limiter with an extinction ratio of 20 dB. As for self-induced mm-wave limiting, the threshold level of such a limiter is too high because of very low absorptance and thus weak heating effect at low temperatures. By using the highest (in this study) mm-wave input power (55 W) and by starting at room temperature, we could not heat the wafer up to θ_c.

In Fig. 3, the mm-wave measurements of the photonic limiter at low power and successively increased temperatures agree well with the transfer-matrix calculations of Fig. 1. The resonance transmittance peak is seen to drop by 40 dB within the 70° to 75° C temperature range, and to completely disappear by the end of the transition (Fig. 3A). When this takes place, the limiter becomes totally reflective (Fig. 3B). Below the transition temperature, the transmittance peak is seen gradually shifting to lower frequencies (Fig. 3C), indicating an increase in the refractive index of VO_2 with the increasing temperature, while its peak value remains unchanged, implying negligible VO_2 absorption below θ_c. The extracted ϵ'_{VO2} and $\epsilon''_{VO2} \approx 0$ are plotted by dashed lines in Fig. 2B. Note that no noticeable change was observed in transmittance spectra of the multilayer without VO_2 coating in the same temperature range.

High-power measurements of the mm-wave limiter

To investigate self-induced mm-wave limiting, time-resolved transmission measurements of the limiter have been carried out with the use of a high-power CW source centered on 95 GHz with an FWHM of 300 MHz (see Materials and Methods). To prevent adverse effects of back-reflected radiation on the mm-wave source, the reflective limiter was tilted by an angle of 6° from the normal incidence direction, thus shifting the transmission resonance to a higher frequency than 95 GHz. Figure 4A shows linear-log plots of the transmitted power $P_T(t)$ for incident Gaussian beams of a waist radius of 16.5 mm and input powers P_0 = 30, 35, 40, 45, and 55 W. For each input power, $P_T(t)$ is seen to initially increase and then decrease with time. This is due to the fact that the transmission resonance shifts to lower frequencies with increasing temperature, in accordance with Fig. 3C, crossing the source frequency of 95 GHz at a time of maximum transmission. In addition, at input powers $P_0 > 30$ W, $P_T(t)$ exhibits a sharp drop associated with the insulator-to-metal transition in the VO_2 layer. The corresponding transition or switching time, t_s, is plotted versus P_0 in the inset; notice that at 30 W input power, the transition is not manifested in $P_T(t)$. The shortest switching time observed in these proof-of-concept measurements was about 7 s at the highest available input power of 55 W. It can be substantially reduced by increasing the input power or ambient temperature or by modifying the limiter design, as discussed in the following sections.

The transition in the VO_2 layer was observed with an forward-looking infrared (FLIR) thermal camera that could distinguish between the dielectric and metallic phases of VO_2 because of their different emissivities in the infrared. Figure 4 (B to D) displays thermal images of the limiter front end at elapsed times indicated by red dashed arrows in Fig. 4A for the incident power of 45 W. The first occurrence of the metallic phase in the center of the VO_2 layer (red spot in Fig. 4C) coincides with the sharp drop in $P_T(t)$. Then, the metallic domain grows in size (Fig. 4D), accompanied by further decrease in $P_T(t)$, until thermal equilibrium is reached. When high input power is no longer present, the VO_2 reverts from the metallic to the dielectric phase after a brief delay (movie S1).

The equilibrium size of the metallic domain and thus the extinction ratio of the limiter increase with the incident power P_0. In contrast, the transmitted power $P_T(t)$ in the steady-state regime (i.e., at longer times) is nearly independent of P_0, as seen in Fig. 4A. This practically important feature is, in fact, due to the Gaussian spatial intensity distribution of the incident beam, $I(r) = (2P_0/\pi r_0^2)\exp(-2r^2/r_0^2)$, where *r* is the radial distance from the center axis of the beam, and r_0 is the beam waist radius, at which the field amplitude falls to 1/*e* of its axial value. Indeed, if the beam is centered on and blocked by an opaque disk of radius *a*, then the transmitted power is $P_T \approx P_0\exp(-2a^2/r_0^2)$ provided the limiter aperture is considerably larger than the disk. Assuming that the value of *a* is determined from $I(r = a) = I_t$, where I_t is the intensity threshold value, the transmitted power is virtually independent of the input power P_0, $P_T \approx \frac{\pi r_0^2 I_t}{2}$. By contrast, in the case of a top-hat incident beam with a near-uniform intensity $I \geq I_t$ within a circular disk, the transmitted power would be suppressed by orders of magnitude shortly after switching of the VO_2 from the dielectric to the metallic state (in accordance with Fig. 1D). Alternatively, substantial suppression of the transmitted intensity can be achieved by using a circular aperture of $r \leq a$ positioned just behind the multilayer, as shown in fig. S3.

Electromagnetic and heat transfer modeling of the mm-wave limiter

To gain deeper insight into the mm-wave limiting process in the photonic limiter, we perform time-domain 3D MULTIPHYSICS simulations of a Gaussian beam propagating through the multilayer of Fig. 1. The electric field component ***E*** of the incident Gaussian

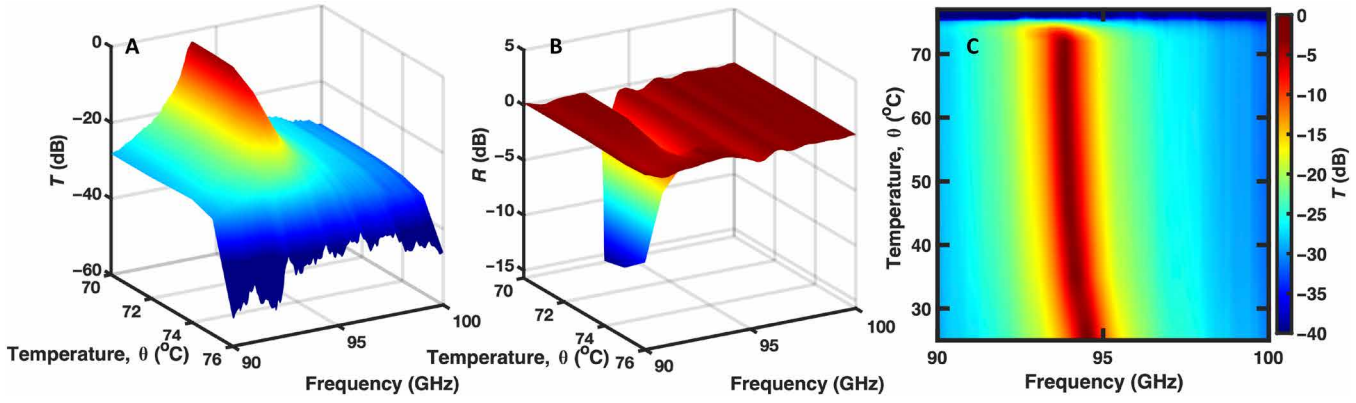

Fig. 3. Mm-wave measurements of the photonic limiter at low input power and increasing temperature. (**A** and **B**) Spectra of transmittance *T* (A) and reflectance *R* (B) of the photonic limiter at input power of ≤10 mW over the resonance spectral range and phase-transition temperature interval. (**C**) Transmittance spectra over the wider temperature range from 27° to 76° C.

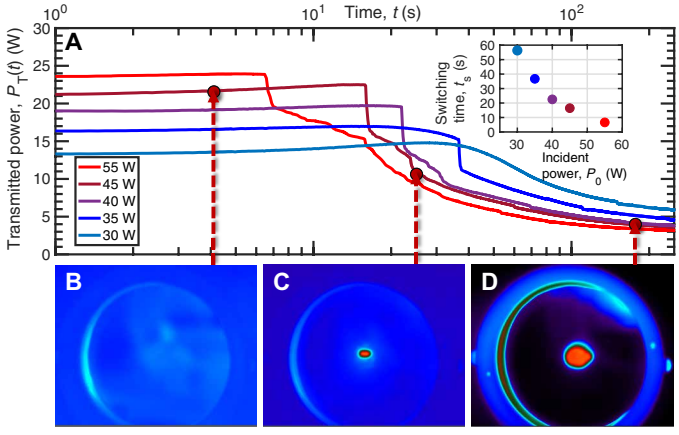

Fig. 4. High-power mm-wave measurements of the photonic limiter. (**A**) Time-varying transmitted power $P_T(t)$ of the photonic limiter following excitation by a CW 95-GHz Gaussian beam with the waist radius r_0 = 16.5 mm and input powers P_0 = 30, 35, 40, 45, and 55 W. Inset: Switching time t_s, corresponding to the onset of the metallic phase in the VO_2 layer, versus the input power P_0. (**B** to **D**) Thermal images of the limiter front end at the elapsed times indicated by the respective dashed arrows in (A), for P_0 = 45 W.

beam (assuming polarization in the radial direction $\hat{\boldsymbol{r}}$ and propagation in the +z direction) is given by

$$\boldsymbol{E}(z,r) = E_0\hat{\boldsymbol{r}}\exp\left(-\frac{r^2}{r_0^2}\right)\exp(-ikz) \quad (1)$$

where E_0 is the on-axis (r = 0) electric field amplitude, $E_0 = \sqrt{4\eta_0 P_0/\pi r_0^2}$, η_0 = 377 Ω is the wave impedance of free space, r_0 = 16.5 mm, and $k = 2\pi/\lambda$ is the wave number for a free-space wavelength λ.

The mm-wave propagation in the case of temperature-dependent permittivity of the VO_2 layer is described by the following set of coupled electromagnetic and thermal equations

$$\nabla\times\boldsymbol{H} = \boldsymbol{j} + \varepsilon\frac{\partial\boldsymbol{E}}{\partial t}, \nabla\times\boldsymbol{E} = -\mu\frac{\partial\boldsymbol{H}}{\partial t} \quad (2)$$

$$\rho c\frac{\partial\theta}{\partial t} = \nabla\cdot(\kappa\nabla\theta) + \dot{Q}$$

where $\boldsymbol{H}$ is the magnetic field component, $\boldsymbol{j} = \sigma\boldsymbol{E}$ is the current density, σ(z, θ) is the electrical conductivity, ε(z, θ) = ε′(z, θ) + iε″(z, θ) is the permittivity, and μ is the permeability. In the second line of equations (2), $\dot{Q} = \frac{1}{2}(Re(\boldsymbol{j}\cdot\boldsymbol{E}) + \omega\varepsilon''|\boldsymbol{E}|^2)$ is the volumetric heat production rate, which can be recast as $\dot{Q} = \frac{1}{2}\omega\varepsilon_0\epsilon''|\boldsymbol{E}|^2$, where ω is the angular frequency, ε_0 is the vacuum permittivity, and ε″ is the imaginary part of the effective relative permittivity, which can be directly obtained from our measurements. The other parameters in Eq. 2 include the specific heat capacity $c(z)$, the mass density ρ(z), and the thermal conductivity κ(z). In the modeling, we assume that the multilayer is thermally insulated on the cylindrical surface (due to the plastic holder) and that the heat flux q across the limiter front and rear ends dissipates by convection, i.e., $q = h(\theta - \theta_0)$, where h = 100 W/(m^{2}K) is the convection heat transfer coefficient (*40*), and θ_0 = 296 K is the ambient temperature. Furthermore, we use the experimentally determined effective relative permittivities of sapphire (ϵ_s) and VO_2 (ϵ_{VO2}) and assume μ to be the magnetic permeability of free space, $\mu = \mu_0$. Last, the thermal properties of the constitutive materials used in the simulations are listed in table S1.

There are two equations in (2) which are solved simultaneously using the coupled Microwave and Heat Transfer modules of COMSOL MULTIPHYSICS software (*41*). Figure 5 shows the computed time-dependent transmitted power $P_T(t)$, reflected power $P_R(t)$, and absorptance $A(t) = (P_0 - P_T(t) - P_R(t))/P_0$ of the limiter following excitation by a 95-GHz Gaussian beam of input powers P_0= 29, 56, 554, and 5540 W. A good agreement between the numerical simulations and the experimental data of Fig. 4 is evident. Specifically, $P_T(t)$ exhibits abrupt, steep decrease once VO_2 has reached θ_c (Fig. 5A). Also, in the steady limiting regime (flat portion of the curves at later times), the input power is reflected to a greater extent than is absorbed (Fig. 5, B and C). We further note in Fig. 5A that the switching time is inversely proportional to the input power, $t_s \propto 1/P_0$, and that at $t > t_s$, the transmitted power decreases inversely with time, $P_T(t) \propto 1/t$ (shown by a dotted black line).

The dependence of t_s on P_0 can be understood from the solution of a heat balance equation (*42*) for the VO_2 layer in the beam center. Assuming for the time being that the temperature distribution in the VO_2-on-sapphire wafer is uniform in the $+z$ direction and neglecting transverse thermal conduction away from the beam center, the heat balance equation is

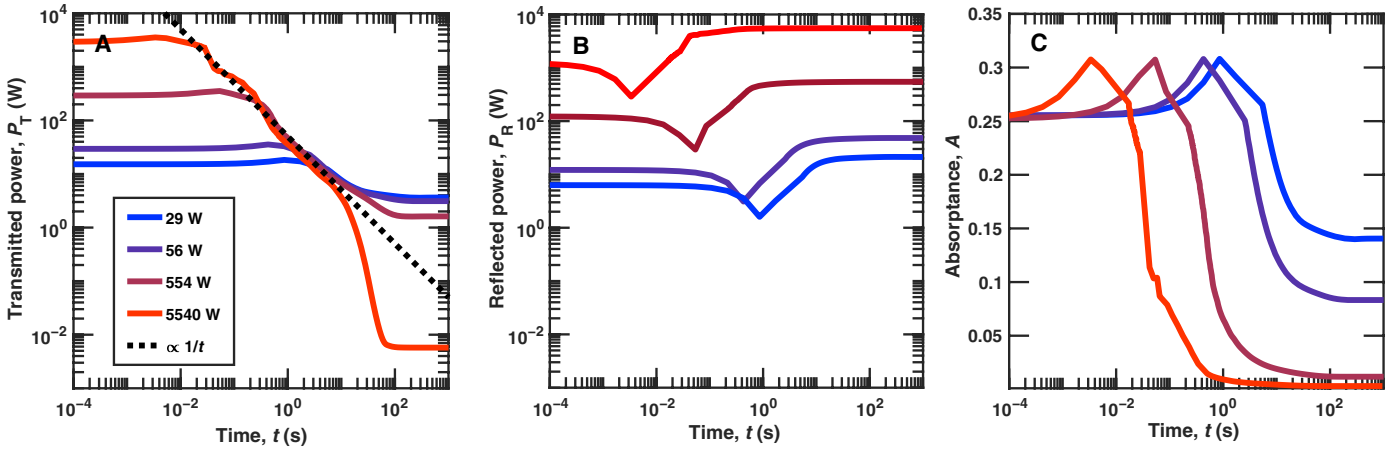

Fig. 5. Simulated temporal response of the photonic limiter under monochromatic excitation. (**A** to **C**) Time evolution of the transmitted power $P_T(t)$ (A), reflected power $P_R(t)$ (B), and absorptance $A(t)$ (C) of the limiter following excitation by a 95-GHz Gaussian beam with the waist radius r_0 = 16.5 mm and input powers P_0 = 29, 56, 554, and 5540 W. The black dashed line in (A) indicates a slope of $P_T(t) \propto 1/t$.

$$C\frac{d\theta}{dt} = AI_{in} + h'(\theta_0 - \theta) \quad (3)$$

where C is the heat capacity per unit surface area, h' is the thermal exchange coefficient, A is the absorptance, and $I_{in} \sim I_0 \exp(L/2\xi)$ is the internal intensity in the middle of the multilayer length L, wherein ξ is the decay length associated with the spatial distribution of the resonant defect mode (Fig. 1E). Assuming that the initial temperature of the VO_2 layer is equal to the ambient temperature, $\theta(t = 0) = \theta_0$, and that C, A, and h' are temperature-independent below θ_c, the solution of Eq. 3 is

$$\theta(t) = \theta_0 + \frac{AI_{in}}{h'}\left(1 - \exp\left(-\frac{h'}{C}t\right)\right) \quad (4)$$

for $\theta_0 \le \theta < \theta_c$. At intensities $I_{in} > h'(\theta_c - \theta_0)/A$, the temperature $\theta(t)$ grows until it reaches the phase transition value θ_c at time

$$t_s = -\frac{C}{h'}\ln\left(1 - \frac{h'}{AI_{in}}(\theta_c - \theta_0)\right) \approx \frac{C(\theta_c - \theta_0)}{AI_{in}} \propto \frac{1}{P_0} \quad (5)$$

Note that in the case of the Gaussian beam of Eq. 1, the larger the radial distance r is, the longer it takes to reach θ_c. As a result, the radius r_m of the metallic domain grows with time according to $t = C(\theta_c - \theta_0)/AI_{in}\exp(-2r_m^2/r_0^2)$, for $t \ge t_s$ (movie S2). Since the transmitted power is $P_T \approx \left(\frac{\pi r_0^2 I_0}{2}\right)\exp(-2r_m^2/r_0^2)$, it decreases with time as $P_T(t) \approx \pi r_0^2 C(\theta_c - \theta_0)/2At\exp(L/2\xi) \propto 1/t$, in agreement with Fig. 5A.

According to Fig. 5, it takes ~100 s for $P_T(t)$ to reach the steady state. By then, $P_T(t)$ has already dropped substantially compared to its initial level. At the input powers $P_0 < 60$ W, the steady-state $P_T(t)$ is independent of P_0 in agreement with the experiment (Fig. 4A). At $P_0 > 60$ W, however, $P_T(t)$ falls further down as the metallic domain becomes comparable to the limiter aperture in size (Fig. 6B). At P_0 = 5540 W, $P_T(t)$ falls by 60 dB, much like in the measurements of transmittance at successively increasing spatially uniform temperatures (Fig. 3A) and of transmitted power through the aperture (fig. S3).

As seen from Fig. 5C, the resonant setting of the multilayer enhances the initial (low-temperature) absorptance by two orders of magnitude compared to the stand-alone VO_2-on-sapphire wafer. In the presence of continuous input power P_0, $A(t)$ rises up to a peak of ~0.32 regardless of P_0 and then falls down to a constant level depending on P_0. This absorptance behavior, which is characteristic of the entire multilayer rather than the stand-alone VO_2-on-sapphire wafer (for comparison, see Fig. 2A), is essential to understanding the mm-wave limiting process in the photonic limiter. The increase in absorptance resulting from the heating effect triggers thermal runaway, in which the VO_2 temperature quickly runs up to θ_c and higher (Fig. 6, A and B), carrying VO_2 through the phase transition. However, because of rapidly increasing reflectivity with the fraction of VO_2 transformed into the metallic phase, the absorptance changes instantly from rising to falling, and the VO_2 layer from heating to cooling, until equilibrium is reached. The equilibrium sets in at a particular metallic fraction of VO_2, at which the limiter is capable of fully dissipating the absorbed power while reflecting most of the input power. If the input power further increases or decreases, then so does the metallic fraction of VO_2 to reset the equilibrium. In contrast, the stand-alone VO_2-on-sapphire wafer exhibits only thermal runaway and lacks equilibrium at $\theta > 69°$ C, because its absorbance at $\theta \ge \theta_c$ is higher than that at $\theta < \theta_c$ (Fig. 2A).

The picture of the self-regulating limiting process in the photonic limiter is further supported by computed temperature time evolution of the VO_2-on-sapphire wafer inside the photonic limiter at input powers of 56 and 554 W shown in Fig. 6. Because of the limiter's axial symmetry, we plot the time-varying radial temperature distributions at the two z-positions: in the VO_2 layer (Fig. 6, A and B) and on the opposite side of the sapphire wafer (Fig. 6, C and D). Below 69° C (shown by a black dashed line), the temperature distributions at these two positions are nearly the same, indicating that the VO_2 layer (assumed to be lossless) is efficiently heated by the absorbing sapphire wafer. At $\theta > 69°$ C, the VO_2 temperature rises faster and higher than in sapphire, particularly at the beam center ($r = 0$) and the higher power of 554 W. The two temperatures peak and fall at the same time despite a temperature gradient across the sapphire wafer, indicating that sapphire is shielded by VO_2 from the incident

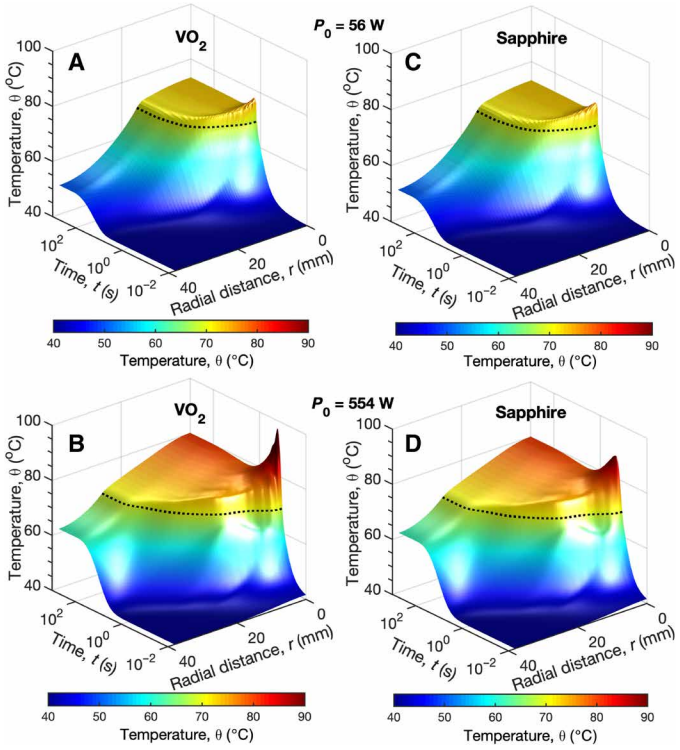

Fig. 6. Simulated temperature evolution of the VO_2-on-sapphire wafer inside the photonic limiter under monochromatic excitation. (**A** and **B**) Radial temperature distribution of the VO_2 layer as a function of elapsed time *t* following excitation by a 95-GHz Gaussian beam with the waist radius r_0 = 16.5 mm and input powers of 56 W (A) and 554 W (B). (**C** and **D**) the same for the opposite (uncoated) side of the sapphire wafer. The black dashed lines correspond to θ_c = 69° C.

beam as the VO_2 is being transformed into the metallic phase. Next, the two temperatures quickly level off, eventually reaching equilibrium temperatures of 75° and 80° C for input powers of 56 and 554 W, respectively, in accordance with Fig. 5 and the subsequent discussion.

DISCUSSION

We have designed and demonstrated a free-space, reflective photonic limiter for the *W* band as an alternative or a complement to electronic limiting circuits used in mm-wave receivers. The proposed photonic limiter is a resonant air/sapphire multilayer structure, incorporating a 150-nm VO_2 layer undergoing an insulator-to-metal transition when heated above the critical temperature, $\theta_c \approx 69°$ C. The multilayer structure is so thin (a few millimeters) that it can be used to cover a wide area, such as a phase antenna array. The limiter acts as a variable reflector, controlled by the incident wave intensity I_0. If I_0 is below a certain threshold level I_t, the VO_2 layer remains in the dielectric state, and the multilayer exhibits high transmittance in a finite frequency band, despite the fact that a small portion of I_0 is absorbed by the multilayer, leading to the initial heating of VO_2. When I_0 exceeds I_t, a fraction of the VO_2 layer transitions into the metallic phase with sharply increased electrical conductivity, rendering the entire multilayer highly reflective. The time t_s before the transition starts is inversely proportional to the incident intensity, $t_s \propto 1/I_0$, after which the multilayer is brought to equilibrium by a combination of positive and negative feedbacks between mm-wave absorption and heating of VO_2. For a given intensity $I_0 \geq I_t$, the equilibrium is determined by the fraction of the VO_2 layer transformed into the metallic phase. At that point, the limiter is capable of safely dissipating a small portion of the incident power absorbed by the limiter, while reflecting the rest of the energy back to space. The high reflectivity (as opposed to absorptance) prevents the limiter from overheating. Moreover, a combination of the resonant conditions and the high contrast in electrical conductivity between the two phases of VO_2 results in a substantial enhancement of the limiter extinction ratio and allows marked reduction in the limiting threshold—both highly desirable features in limiting applications.

The limiter properties, such as operating frequency, bandwidth, threshold level, and switching time, are determined by the limiter design, ambient conditions, and incident power density. In particular, as long as the VO_2 nanolayer is in the dielectric phase, most of the resonant absorption occurs in the sapphire substrate, while the VO_2 contributions to the absorption and heating processes remain negligible. The relatively large thickness of the sapphire substrate (~0.5 mm) results in its large heat capacity, which explains the long switching times of the limiter. If the damage inflicted by HPM is thermal in origin, then a critically important characteristic of the free-space limiter is the energy density passed through the limiter before the limiter blocks the input radiation, $U = I_0 t_s$, where t_s is given by Eq. 5. It thus turns out that if the incident intensity I_0 is well above the limiting threshold, the value of U is virtually independent of I_0, $U \approx C(\theta_c - \theta_0)/A$, provided that t_s is much shorter than the temperature relaxation time of the limiter. Given the specific parameters of our limiter and the ambient temperature, the total transmitted energy density U during the limiter switching time t_s is ~22.5 J/cm^2. One way to substantially reduce both the switching time t_s and the passed energy density U would be to deposit a resistive nanolayer or nanostructure (*43*) on the top of the VO_2. The heat capacity of the resistive nanolayer can be much smaller than that of the sapphire substrate (e.g., by four orders of magnitude in the case of In_2O_5Sn), and the heat released in the resistive nanolayer will be almost instantly transferred to the VO_2 nanolayer. Preliminary estimates show the reduction in t_s and U of more than three orders of magnitude, particularly for the incident intensity I_0 well above the limiting threshold (it can still be well below the damage threshold). The limiter performance is also determined by spatial and temporal characteristics of the incident radiation. In particular, in the case of CW Gaussian beam, the output power of the limiter operating above the threshold appears virtually independent of the input power because of nonuniform heating of the VO_2 layer.

MATERIALS AND METHODS

Thin-film deposition and structural analysis

The VO_2 thin film was deposited in a Neocera Pioneer 180 Pulse Laser Deposition system with a KrF excimer laser (Coherent COMPexPro 110, λ = 248 nm, 10-ns pulse duration, 10-Hz repetition rate) applied for the ablation of a high-purity vanadium disk. The chamber base pressure of a 5% O_2/95% Ar gas mixture was maintained at 25 mtorr during the deposition. The 76.2-mm double-side-polished C-cut (006) sapphire substrate was held at 600° C. X-ray diffraction (XRD) analysis of the VO_2 films was carried out using a PANalytical X'Pert diffractometer with a hybrid monochromator for Cu $K\alpha_1$ radiation (λ = 1.54056 A) at room temperature. The presence of highly oriented

monoclinic VO_2 crystalline phase is indicated by the characteristic XRD peaks (020) and (040) at 39.87° and 85.97°, respectively (fig. S1) (*44*). The average VO_2 crystalline grain size about 110 nm was found from the Scherrer equation for the FWHM (β) of the (020) peak (*45*). A VO_2 film thickness of approximately 150 nm was measured with SEM.

Mm-wave spectral measurements

Mm-wave field spectra of the photonic limiter and complex permittivities of its constitutive components were obtained using a *W*-band, high-temperature, free-space measurement apparatus (*46*). The measurement system consisted of an Agilent 5222A performance network analyzer (PNA), N5261A millimeter head controller, and a set of OML V10VNA-T/R frequency extender heads (one for each port) serving to boost the output of the PNA base unit to the *W*-band frequencies (75 to 110 GHz). A matched set of custom-designed, lensed horn antennas was used for launching and receiving a Gaussian mm-wave beam (waist radius of 16.5 mm) transmitted via and reflected from the sample. The sample was located in the center of a Mellen tube furnace with an overall length and diameter of 32 and 15 cm, respectively, and a 15-cm-long, uniform heating region centered along the axial length of the furnace. A silicon carbide composite sample holder was used for the measurements. The temperature was controlled with an E-type thermocouple embedded in the sample holder immediately adjacent to the outer radius of the sample. In the temperature range from 27° to 110° C, the thermocouple had an accuracy of 1.0° C.

High-power mm-wave measurements

For higher-power free-space measurements, a CPI VKB2463L2 Extended Interaction Klystron (EIK) power amplifier was used to provide a CW 95-GHz signal. EIK input and output mm-wave power was sampled using calibrated directional couplers and then measured using diode-based detectors. The input mm-wave drive signal was controlled with a LabVIEW-based feedback circuit to maintain a consistent mm-wave power output over extended periods of time, which could otherwise drop because of heating of components. The EIK mm-wave output was coupled into the same lensed antenna that was used with the network analyzer measurement setup, to form a Gaussian beam directed into a shielded anechoic chamber and focused at the center of the sample being interrogated. At a peak power gain, the maximum incident power of the Gaussian mm-wave beam was 55 W.

MULTIPHYSICS simulations

Equation 2 was solved numerically, using the coupled Microwave and Heat Transfer modules of a finite-element software package from COMSOL MULTIPHYSICS (*41*) and a 2D axisymmetric model, capturing all the features of the 3D problem with axial (cylindrical) symmetry. In the simulations, we used a varying mesh density (fig. S4). The thin sapphire and air-gap layers were partitioned with the mesh density increased toward the center of the limiter, while the center sapphire and air-gap layers toward the VO_2 layer. The convergence of the results has been evaluated with a tolerance factor of 0.1%. We then repeated the calculations by doubling the number of mesh points to guarantee the accuracy of the converged numerical solutions. The mm-wave source was modeled with a surface current density line producing the Gaussian beam, which was located 1.5 mm away from the front end of the multilayer inside the far-field air domain. The wave propagation was modeled using PML boundary conditions to avoid the back reflections from the boundaries of the geometry.

SUPPLEMENTARY MATERIALS

Supplementary material for this article is available at https://science.org/doi/10.1126/sciadv.abh1827

REFERENCES AND NOTES

1. T. S. Rappaport, S. Sun, R. Mayzus, H. Zhao, Y. Azar, K. Wang, G. N. Wong, J. K. Schulz, M. Samimi, F. Gutierrez Jr., Millimeter wave mobile communications for 5g cellular: It will work! *IEEE Access* **1**, 335–349 (2013).
2. J. G. Andrews, S. Buzzi, W. Choi, S. V. Hanly, A. Lozano, A. C. K. Soong, J. C. Zhang, What will 5G be? *IEEE J. Sel. Areas Commun.* **32**, 1065–1082 (2014).
3. L. Yujiri, M. Shoucri, P. Moffa, Passive millimeter wave imaging. *IEEE Microw. Mag.* **4**, 39–50 (2003).
4. J. C. K. Wells, *Multigigabit Microwave and Millimeter-Wave Wireless Communications* (Artech House Publishers, 2010).
5. C. Iovescu, S. Rao, The fundamentals of millimeter-wave sensors. (Publication SPYY005, Texas Instruments, 2017); www.mouser.ee/pdfdocs/mmwavewhitepaper.pdf.
6. W. A. Radasky, C. E. Baum, M. W. Wik, Introduction to the special issue on high-power electromagnetics (HPEM) and intentional electromagnetic interference (IEMI). *IEEE Trans. Electromagn. Compat.* **46**, 314–321 (2004).
7. M. G. Backstrom, K. G. Lovstrand, Susceptibility of electronic systems to high-power microwaves: Summary of test experience. *IEEE Trans. Electromagn. Compat.* **46**, 396–403 (2004).
8. R. Hsu, A. Ayazi, B. Houshmand, B. Jalali, All-dielectric photonic-assisted radio front-end technology. *Nat. Photonics.* **1**, 535–538 (2007).
9. J. Benford, J. A. Swegle, E. Schamiloglu, *High Power Microwaves* (Taylor & Francis, ed. 2, 2007).
10. E. Schamiloglu, High power microwave sources and applications, in *Proceedings of the IEEE MTT-S International Microwave Symposium Digest* (Jun. 2004), vol. 2, pp. 1001–1004.
11. R. Cory, *PIN-Limiter Diodes Effectively Protect Receivers* (EDN Magazine, 17 December, 2004), pp. 50–64.
12. K. Gong, H. Feng, R. Zhan, A. Z. H. Wang, A study of parasitic effects of ESD protection on RF ICs. *IEEE Trans. Microw. Theory Techn.* **50**, 393–402 (2002).
13. R. W. Heath, N. González-Prelcic, S. Rangan, W. Roh, A. M. Sayeed, An overview of signal processing techniques for millimeter wave MIMO systems. *IEEE J. Sel. Top. Signal Process.* **10**, 436–453 (2016).
14. A. Hirata, H. Harada, T. Nagatsuma, 120-GHz wireless link using photonic techniques for generation, modulation, and emission of millimeter-wave signals. *J. Light. Technol.* **21**, 2145–2153 (2003).
15. J. McKinney, Photonics illuminates the future of radar. *Nature* **507**, 310–312 (2014).
16. P. Ghelfi, F. Laghezza, F. Scotti, G. Serafino, A. Capria, S. Pinna, D. Onori, C. Porzi, M. Scaffardi, A. Malacarne, V. Vercesi, E. Lazzeri, F. Berizzi, A. Bogoni, A fully photonics-based coherent radar system. *Nature* **507**, 341–345 (2014).
17. X. Zou, B. Lu, W. Pan, L. Yan, A. Stöhr, J. Yao, Photonics for microwave measurements. *Laser Photonics Rev.* **10**, 711–734 (2016).
18. X. Xie, R. Bouchand, D. Nicolodi, M. Giunta, W. Hänsel, M. Lezius, A. Joshi, S. Datta, C. Alexandre, M. Lours, P.-A. Tremblin, G. Santarelli, R. Holzwarth, Y. L. Coq, Photonic microwave signals with zeptosecond-level absolute timing noise. *Nat. Photonics* **11**, 44–47 (2017).
19. D. G. Georgiadou, J. Semple, A. A. Sagade, H. Forstén, P. Rantakari, Y.-H. Lin, F. Alkhalil, A. Seitkhan, K. Loganathan, H. Faber, T. D. Anthopoulos, 100 GHz zinc oxide Schottky diodes processed from solution on a wafer scale. *Nat. Electron.* **3**, 718–725 (2020).
20. L. W. Tutt, T. F. Boggess, A review of optical limiting mechanisms and devices using organics, fullerenes, semiconductors and other materials. *Prog. Quantum. Electron.* **17**, 299–338 (1993).
21. M. J. Miller, A. G. Mott, B. P. Ketchel, General optical limiting requirements. *Proc. SPIE* **3472**, 24–29 (1998).
22. E. W. Van Stryland, Y. Y. Wu, D. J. Hagan, M. J. Soileau, K. Mansour, Optical limiting with semiconductors. *J. Opt. Soc. Am. B* **5**, 1980–1988 (1988).
23. L. W. Tutt, A. Kost, Optical limiting performance of C_{60} and C_{70} solutions. *Nature* **356**, 225–226 (1992).
24. P. Chen, X. Wu, X. Sun, J. Lin, W. Ji, K. L. Tan, Electronic structure and optical limiting behavior of carbon nanotubes. *Phys. Rev. Lett.* **82**, 2548–2551 (1999).
25. T. Boggess, A. Smirl, S. Moss, I. Boyd, E. Van Stryland, Optical limiting in GaAs. *IEEE J. Quantum Electron.* **21**, 488–494 (1985).
26. E. Makri, H. Ramezani, T. Kottos, I. Vitebskiy, Concept of a reflective power limiter based on nonlinear localized modes. *Phys. Rev. A* **89**, 031802 (2014).

27. E. Makri, T. Kottos, I. Vitebskiy, Reflective optical limiter based on resonant transmission. *Phys. Rev. A* **91**, 043838 (2015).
28. J. H. Vella, J. H. Goldsmith, A. T. Browning, N. I. Limberopoulos, I. Vitebskiy, E. Makri, T. Kottos, Experimental realization of a reflective optical limiter. *Phys. Rev. Appl.* **5**, 064010 (2016).
29. S. Suwunnarat, R. Kononchuk, A. Chabanov, I. Vitebskiy, N. I. Limberopoulos, T. Kottos, Enhanced nonlinear instabilities in photonic circuits with exceptional point degeneracies. *Photonics Res.* **8**, 737–744 (2020).
30. R. Thomas, A. A. Chabanov, I. Vitebskiy, T. Kottos, Light-induced optical switching in an asymmetric metal-dielectric microcavity with phase-change material. *EPL* **126**, 64003 (2019).
31. N. Antonellis, R. Thomas, M. A. Kats, I. Vitebskiy, T. Kottos, Nonreciprocity in photonic structures with phase-change components. *Phys. Rev. Appl.* **11**, 024046 (2019).
32. S. D. Ha, Y. Zhou, A. E. Duwel, D. W. White, S. Ramanathan, Quick switch: Strongly correlated electronic phase transition systems for cutting-edge microwave devices. *IEEE Microw. Mag.* **15**, 32–44 (2014).
33. J. Givernaud, A. Crunteanu, J.-C. Orlianges, A. Pothier, C. Champeaux, A. Catherinot, P. Blondy, Microwave power limiting devices based on the semiconductor-metal transition in vanadium-dioxide thin films. *IEEE Trans. Microw. Theory Tech.* **58**, 2352–2361 (2010).
34. U. K. Chettiar, N. Engheta, Modeling vanadium dioxide phase transition due to continuous-wave optical signals. *Opt. Express* **23**, 445–451 (2015).
35. C. Wan, E. H. Horak, J. King, J. Salman, Z. Zhang, Y. Zhou, P. Roney, B. Gundlach, S. Ramanathan, R. H. Goldsmith, M. A. Kats, Limiting optical diodes enabled by the phase transition of vanadium dioxide. *ACS Photonics* **5**, 2688–2692 (2018).
36. J. Rozen, R. Lopez, R. F. Haglund, L. C. Feldman, Two-dimensional current percolation in nanocrystalline vanadium dioxide films. *Appl. Phys. Lett.* **88**, 081902 (2006).
37. M. M. Qazilbash, M. Brehm, B.-G. Chae, P.-C. Ho, G. O. Andreev, B.-J. Kim, S. J. Yun, A. V. Balatsky, M. B. Maple, F. Keilmann, H.-T. Kim, D. N. Basov, Mott transition in VO_2 revealed by infrared spectroscopy and nano-imaging. *Science* **318**, 1750–1753 (2007).
38. P. J. Hood, J. F. DeNatale, Millimeter-wave dielectric properties of epitaxial vanadium dioxide thin films. *J. Appl. Phys.* **70**, 376–381 (1991).
39. P. Yeh, *Optical Waves in Layered Media* (Wiley, 1988).
40. J. H. Whitelaw, Convective heat transfer (Thermopedia, 2011); http://thermopedia.com/content/660/.
41. *COMSOL Multiphysics Model Library* (COMSOL AB, v.5.2, 2015).
42. T. L. Bergman, A. S. Lavine, F. P. Incropera, D. P. Dewitt, *Fundamentals of Heat and Mass Transfer* (Wiley, ed. 7, 2011).
43. L. Kong, Z. Li, L. Liu, R. Huang, M. Abshinova, Z. Yang, C. B. Tang, P. Tan, C. Deng, S. Matitsine, Recent progress in some composite materials and structures for specific electromagnetic applications. *Int. Mater. Rev.* **58**, 203–259 (2013).
44. H. Kim, N. Charipar, M. Osofsky, S. B. Qadri, A. Piqué, Optimization of the semiconductor-metal transition in VO_2 epitaxial thin films as a function of oxygen growth pressure. *Appl. Phys. Lett.* **104**, 081913 (2014).
45. A. J. Littlejohn, Y. Yang, Z. Lu, E. Shin, K. C. Pan, G. Subramanyam, V. Vasilyev, K. Leedy, T. Quach, T.-M. Lu, G.-C. Wang, Naturally formed ultrathin V_2O_5 heteroepitaxial layer on VO_2 /sapphire (001) film. *Appl. Surf. Sci.* **419**, 365–372 (2017).
46. M. S. Hilario, B. W. Hoff, B. Jawdat, M. T. Lanagan, Z. W. Cohick, F. W. Dynys, J. A. Mackey, J. M. Gaone, *W*-band complex permittivity measurements at high temperature using free-space methods. *IEEE Trans. Compon. Packaging Manuf. Technol.* **9**, 1011–1019 (2019).
47. Valley Design Corp. Properties of sapphire wafers and substrates. (Valley Design Corp., 2015); http://valleydesign.com/sappprop.htm.
48. Y. S. Touloukian, P. E. Liley, S. C. Saxena, *Thermophysical Properties of Matter - The TPRC Data series. Vol. 3. Thermal Conductivity - Nonmetallic Liquids and Gases* (Defense Technical Information Center, 1970).
49. C. Leroux, G. Nihoul, G. Van Tendeloo, From $VO_2(B)$ to $VO_2(R)$: Theoretical structures of VO_2 polymorphs and in situ electron microscopy. *Phys. Rev. B* **57**, 5111–5121 (1998).
50. C. N. Berglund, H. J. Guggenheim, Electronic properties of VO_2 near the semiconductor-metal transition. *Phys. Rev.* **185**, 1022–1033 (1969).

Acknowledgments: We thank K. Leedy and E. Shin for technical help with the PLD system and helpful discussions. **Funding:** This research has been supported by the Air Force Office of Scientific Research (FA9550-19-1-0359, FA9550-21-1-0145, LRIR 21RYCOR019, and LRIR 20RDCOR022), Office of Naval Research (N00014-19-1-2480), and DARPA (HR00111820042).
Author contributions: R.K. assembled the limiter prototype, analyzed the data, and prepared the figures for the manuscript. R.K. and S.S. performed the numerical simulations. V.V. grew and characterized the VO_2 thin film. A.E.B., M.S.H., and B.W.H. devised the experimental protocols, built the mm-wave setup, and conducted the experiments. A.A.C., T.K., and I.V. proposed the project and wrote the draft. All the coauthors discussed the results and contributed to the final version of the manuscript. **Competing interests:** The authors declare that they have no competing interests. **Data and materials availability:** All data needed to evaluate the conclusions in the paper are present in the paper and/or the Supplementary Materials.

Submitted 20 February 2021
Accepted 22 November 2021
Published 14 January 2022
10.1126/sciadv.abh1827